

Document Version

Final published version

Licence

CC BY

Citation (APA)

Mahadevan, G., Sabooni, S., Popovich, V., Kestens, L. A. I., & Hermans, M. (2026). Characterizing the effect of GB misorientation on liquid metal embrittlement crack path of resistance spot welded TWIP steel. *Materialia*, 48, Article 102776. <https://doi.org/10.1016/j.mtla.2026.102776>

Important note

To cite this publication, please use the final published version (if applicable).
Please check the document version above.

Copyright

In case the licence states "Dutch Copyright Act (Article 25fa)", this publication was made available Green Open Access via the TU Delft Institutional Repository pursuant to Dutch Copyright Act (Article 25fa, the Taverne amendment). This provision does not affect copyright ownership.
Unless copyright is transferred by contract or statute, it remains with the copyright holder.

Sharing and reuse

Other than for strictly personal use, it is not permitted to download, forward or distribute the text or part of it, without the consent of the author(s) and/or copyright holder(s), unless the work is under an open content license such as Creative Commons.

Takedown policy

Please contact us and provide details if you believe this document breaches copyrights.
We will remove access to the work immediately and investigate your claim.



Full Length Article

Characterizing the effect of GB misorientation on liquid metal embrittlement crack path of resistance spot welded TWIP steel

Gautham Mahadevan^{a,*} , Soheil Sabooni^c, Vera Popovich^a, Leo A.I. Kestens^{a,b}, Marcel Hermans^a 

^a Department of Materials Science and Engineering, Delft University of Technology, Mekelweg 2, 2628 CD Delft, the Netherlands

^b Department of Electromechanics, Systems and Metals Engineering, Ghent University, Technologiepark 46, 9052 Gent, Belgium

^c Tata Steel Nederland Technology B.V., P.O. Box 1000, 1970 CA IJmuiden, the Netherlands

ARTICLE INFO

Keywords:

Liquid metal embrittlement
Resistance spot welding
TWIP steel
Misorientation
Coincidence site lattice
Grain boundary engineering
Zn diffusion

ABSTRACT

Liquid metal embrittlement (LME) during resistance spot welding (RSW) of Zn-coated twinning-induced plasticity (TWIP) steel results in intergranular cracking driven by the interaction of liquid Zn, tensile stress, and the grain boundary (GB) network. This study investigates how GB misorientation and orientation relative to the electrode force loading axis influence the LME crack path across six weld times from 700 ms to 1700 ms. A comparative framework was developed in which, at each triple junction along the LME crack, the misorientation and angle relative to the loading axis of the chosen LME grain boundary are evaluated against those of the unchosen LME-free grain boundary. $\Sigma 3$ coherent twin boundaries were LME-free at all weld times regardless of their orientation to the stress axis. Non-twin coincident site lattice (CSL) boundaries ($\Sigma 5$ to $\Sigma 41$) were predominantly LME-free at low weld times but progressively became LME GBs at high weld times, when their stress normalisation factor exceeded that of the competing boundary. The fraction of triple junctions where the LME grain boundary had the higher stress normalisation factor increased from 58% at 700 ms to 91% at 1700 ms, while the preference for the higher-misorientation-angle boundary declined from 73% to 56% over the same range. An LME susceptibility index incorporating grain boundary energy, temperature-dependent Zn diffusivity, and stress alignment is proposed as a framework for predicting crack path selection and guiding grain boundary engineering strategies (GBE) to reduce LME in resistance spot welded TWIP steel.

1. Introduction

In recent decades, the automotive industry has focused on decreasing vehicle weight and fuel consumption while maintaining strength and crash resistance in order to reduce the overall carbon footprint [1]. To meet these requirements, advanced high-strength steels (AHSS) are increasingly used, as they combine high strength and ductility for structural automotive components [2–5]. Twinning induced plasticity (TWIP) steel is one such AHSS used in the automotive industry. Resistance spot welding (RSW) is the main joining method in automotive manufacturing, with each vehicle typically containing between 3000 and 5000 spot welds. During RSW, a weld nugget is created through the combined action of electrode force and Joule heating, which leads to melting and subsequent solidification at the interface between the steel sheets that are joined. The welding cycle is governed by parameters such as welding current, electrode force, electrode geometry, squeeze time,

weld time, and hold time. The process proceeds in three stages. First, in the squeeze time, the electrode force is applied without welding current to keep the sheets in contact with each other. Next, during the weld time (WT), the applied force is maintained while current passes through the sheets and generates resistive heating to melt the interface between the sheets. Finally, in the hold time, the current is switched off and the force is maintained by water-cooled electrodes to form a metallurgical bond between the steel sheets [6]. During RSW, the combined thermal and stress conditions can cause the Zn coating to melt and penetrate grain boundaries (GBs) in the solid steel substrate. This penetration can lead to crack formation, a phenomenon known as liquid metal embrittlement (LME) [7]. LME is a critical concern for advanced high-strength steels such as TWIP steel, as each weld can act as a potential failure site in automotive applications. Despite their high strength and ductility, TWIP steels have been shown in multiple studies to be highly susceptible to LME [8–11]. LME crack initiation and growth are governed by the

* Corresponding author.

E-mail address: g.mahadevan@tudelft.nl (G. Mahadevan).

<https://doi.org/10.1016/j.mtla.2026.102776>

Received 11 May 2026; Accepted 2 June 2026

Available online 3 June 2026

2589-1529/© 2026 The Authors. Published by Elsevier Inc. on behalf of Acta Materialia Inc. This is an open access article under the CC BY license (<http://creativecommons.org/licenses/by/4.0/>).

combined influence of stress, temperature, strain, and steel microstructure. In addition, spatial variations of stress, temperature, and microstructure within the weld increase the complexity of the phenomenon and contribute to the formation of different types of LME cracks [8,12–15].

Several mechanisms have been proposed depending on the solid/liquid metal system involved. For the Fe-Zn system, stress-assisted grain boundary (GB) diffusion is considered the dominant micro-mechanism. Stress-assisted LME models are derived from the Rehbinder effect, in which liquid Zn penetrates GBs, reduces the surface energy of the steel, and promotes embrittlement once a critical stress level is exceeded [16–18]. Since stress-assisted GB diffusion is considered to play a dominant role in the Fe-Zn system, the characteristics of the GBs influence LME crack initiation and propagation. The weld times investigated in this study (700 ms to 1700 ms) are sufficient for liquid Zn to melt, diffuse along GBs, and cause embrittlement via the Rehbinder mechanism [19,20]. Among these characteristics, GB misorientation is a crystallographic parameter that defines the orientation relationship between adjacent grains [17,20,21]. Because GB structure and energy are directly related to misorientation, variations in misorientation may affect the susceptibility of specific boundaries to Zn diffusion under the combined action of stress and temperature during RSW [16]. Therefore, understanding how GB misorientation influences LME behaviour is essential for clarifying crack path selection and identifying which boundaries are more likely to act as preferential pathways for crack growth.

Bhattacharya et al. studied the influence of starting microstructure on the severity of embrittlement in Zn coated AHSS [22]. The study concluded that the prior austenitic GBs (PAGBs) provided low energy paths for crack propagation and hence are preferred for embrittlement. The DP steel's lower area fraction of PAGBs, because of the inter-critical annealing, reduces the availability of low energy paths for crack propagation [22]. Although misorientation angles were measured between grains on either side of the crack, the number of GBs misorientation angles analysed was insufficient to ascertain which grains were preferred for crack propagation. For a given microstructure, it was observed that for a misorientation angle greater than 15° , a lower critical stress is required for LME, due to the increase in grain boundary energy [23]. Atomistic models and TEM observations were employed to study the kinetics of liquid metal penetration in the Al-Ga system. The observations of this study quantitatively verified that a low unit cell volume of the coincident site lattice (CSL) Σ GBs enabled much slower liquid metal penetration compared to high Σ GBs. Razmpoosh et al. validated these observations for a Fe-Zn system, and investigated the influence of GB misorientation angle and crystallographic plane on LME crack propagation and LME susceptibility of FCC Fe-Zn couple [24]. A trace analysis technique using EBSD was applied to LME susceptible GBs, where it was concluded that the orientation of GB planes had a significant effect on the crack path. It was observed that liquid Zn penetrated the GBs of the Fe matrix along high-index planes and the (5 3 1) plane had the highest susceptibility to exhibit LME [24]. According to Razmpoosh et al., LME cracks in Fe-Zn systems tend to follow high-angle random austenite GBs, and the susceptibility of these boundaries depends on the tensile stress component normal to the boundary plane, with a threshold stress of roughly 80% of the yield strength required to trigger liquid Zn penetration and grain-boundary decohesion [24]. According to Gong et al., the applied stress axis controls both the depth and rate of liquid metal penetration along GBs once a critical normal stress on the boundary is exceeded [25]. According to Hong et al., the susceptibility of individual GBs to embrittle is governed by the stress component perpendicular to the grain-boundary plane together with the grain-boundary character, so that high-angle random, high-index boundaries with larger excess free volume are most prone to embrittlement, whereas low- Σ CSL boundaries remain comparatively LME resistant [26]. Bertolo et al. studied Zn-galvanised TWIP steel and deliberately induced LME cracks, then reconstructed the crack path

relative to the austenite grain boundary network [27]. Using EBSD mapping and tracing the crack path, the study showed that intergranular LME cracks preferentially propagate along HAGBs and avoid low- Σ CSL boundaries. In this framework, the global tensile axis defines the stress state, and the orientation of individual boundaries relative to this axis determines the resolved normal stress and their susceptibility to LME.

Although previous studies have examined the role of GB character in LME crack propagation, how these relationships evolve under the conditions present during RSW has not been systematically studied. In particular, the combined influence of GB misorientation and the orientation of GBs relative to the loading axis during welding remains unclear. Furthermore, the extent to which welding parameters affect these relationships during crack propagation is not well understood. Therefore, this study investigates how GB misorientation and GB orientation with respect to the loading axis influence LME crack paths, and how these effects change under different welding parameters during RSW.

2. Material and Methods

2.1. Materials

A heterogeneous triple-stack configuration was used for the RSW experiments. The top sheet was galvanized, cold-rolled austenitic TWIP steel with a thickness of 1.23 mm and an approximate Zn coating thickness of $12 \mu\text{m}$. This TWIP steel is known to be susceptible to LME [8–10,28].

During RSW, the TWIP sheet was placed on top of two DX54 steel sheets, each with a thickness of 1.5 mm and an average Zn coating thickness of approximately $15 \mu\text{m}$, as illustrated in Fig. 1. DX54 is a deep-drawing steel grade that is used for its high forming ability DX54 sheets were used in the triple-stack configuration to increase the heat input during welding and thereby promote the formation of LME cracks [29]. All steel sheets were coating with Zn.

The chemical composition of the main alloying elements in the TWIP steel is listed in Table 1. The composition of the DX54 sheet is listed in Table 2. XRF was used to ascertain the composition of the steel sheets. The balance for both compositions is Fe.

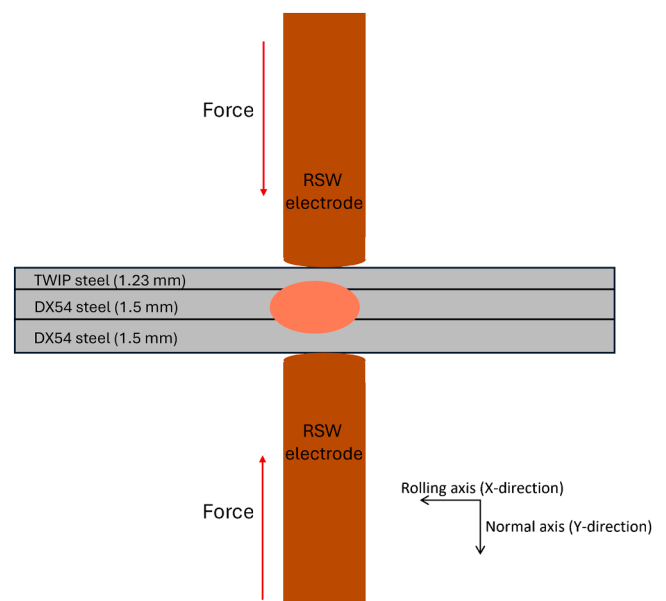


Fig. 1. Schematic representation of the RSW setup showing the sample coordinate system.

Table 1
Composition of alloying elements in TWIP steel in wt%.

Mn	Al	C	Ni	Cr, S, Si, Ti, P
17.3	1.49	0.61	0.36	0.24

Table 2
Composition of alloying elements in DX54 steel in wt%.

C	Si	Mn	P
0.12	0.5	0.6	0.1

2.2. Welding setup

Spot welds were produced using a 1000 MHz MFDC spot welding machine operating under constant current regulation. The welding parameters used in this study are summarized in Table 3 and were selected following internal optimization. During welding, the electrode force, welding current, squeeze time, and hold time were kept constant. The welding current was chosen as the highest value that did not produce expulsion at a weld time (WT) of 1700 ms.

ISO5821 F1-16-20-6 CuCr1Zr electrodes were used and tip-dressed prior to welding. A total of eight weld times were investigated, ranging from 300 ms to 1700 ms with intervals of 200 ms, and four samples were produced for each weld time condition.

2.3. Characterization

LME cracks on the surface of the spot welds were first identified using a VHX7000N optical microscope. Regions containing cracks were then selected for cross-sectional analysis. For SEM preparation, the samples were ground using progressively finer grit sandpapers and subsequently polished using 3 μm silica paste, followed by 1 μm diamond paste and OP-S liquid to produce a smooth surface suitable for imaging. Microstructural characterization was performed using a JEOL® IT800SHL™ scanning electron microscope equipped with a field emission gun, operated at 10 kV with a beam current of 3.2 nA. The microscope was fitted with an Oxford Instruments® Maxim 100™ detector, which was used to carry out Energy Dispersive Spectroscopy (EDS) and Electron Backscatter Diffraction (EBSD) analyses. EBSD data were post-processed using EDAX-OIM Analysis™ v8 software. Grains were defined using a tolerance angle of 15° and a minimum grain size of 5 pixels with multiple rows required. Taylor factor maps were calculated considering the 12 slip systems in FCC Fe. The critical resolved shear stress (CRSS) was set to the default value of 0.2, and the Cauchy strain tensor was defined as 1, -0.5, and 0.5, corresponding to a uniaxial tensile axis along the A1 direction (y-direction in this study), as prescribed by Bertolo et al [27].

2.4. FEA model

Finite element analysis (FEA) of the RSW process was performed using SORPAS to evaluate the evolution of stresses in the weld region. The simulations focused on the weld shoulder area, where LME cracks were observed in the experiments. The model was conFig.d to replicate the experimental welding conditions, including sheet materials, sheet thicknesses, electrode geometry, and applied welding parameters.

Table 3
RSW process parameters.

Welding current (kA)	Electrode force (kN)	Squeeze time (ms)	Hold time (ms)	Weld time (ms)
7.4	4.5	150	150	300, 500, 700, 900, 1100, 1300, 1500 and 1700

Temperature dependent thermo-mechanical properties of the steel sheets were obtained from JMatPro and implemented in the simulation. The simulations provided the evolution of stress components in the x and y directions as a function of time at the weld shoulder. These stress-time profiles were used to assess the orientation of the loading axis relative to the GBs in the TWIP steel.

3. Results

3.1. Microstructure characterization of LME cracks

Fig. 2 presents the EBSD image quality (IQ) maps of LME cracks obtained from the different RSW conditions, covering weld times from 700 ms to 1700 ms. No LME cracks were observed at weld times of 300 ms and 500 ms, so these weld conditions are not part of the study. The IQ maps also reveal the GB network in the cross-section. In the Fig., black lines represent high angle GBs (HAGBs) with misorientations between 15° and 65°, while blue lines denote low angle GBs (LAGBs) with misorientations between 5° and 15°. $\Sigma 3$ CSL GBs are highlighted in red and represent twin boundaries, which are predominant in TWIP steel. The LME crack in Fig. 2 at a weld time of 1700 ms is observed to propagate into the weld fusion region.

Fig. 3 also shows the variation in LME crack depth and width as a function of weld time. Both crack depth and width increase with increasing weld time, which can be attributed to the higher heat input during welding.

3.2. Analysis framework

The misorientation analysis framework used in this study is illustrated schematically in Fig. 4. This framework is adapted from the study by Bertolo et al [27]. Fig. 4(a) shows a schematic representation of the grain structure and GB network in the TWIP steel RSW cross-section. Two distinct categories of GB misorientations are identified and measured. The first category, indicated by blue arrows, are the misorientations between adjacent grains separated by the LME crack - that is, the GBs along which LME crack propagation occurs. These are referred to henceforth as 'LME GBs'. In the schematic, this corresponds to the misorientations between grain pairs G1/G2, G2/G3, G3/G4, G4/G5, and G5/G6. The second category, indicated by red arrows, comprises the misorientations between grains that form part of a triple junction that the LME crack passes through, but did not propagate - that is, the GBs at each triple junction that were available to the crack as an alternative path but were not selected. These are referred to henceforth as 'LME-free GBs'. In the schematic, these correspond to grain pairs G1/G3, G2/G4, G3/G5, and G4/G6. This paired measurement at each triple junction - one LME GB and one LME-free GB forms the basis of the comparative crack path analysis. By comparing the LME and LME-free GBs, the study aims to understand how the GB character affects the LME crack path under changing RSW parameters.

The loading direction in Fig. 4(a) corresponds to the direction of the applied electrode force during RSW, which generates compressive stresses along this axis. The magnitude of the stresses in the y-axis (loading direction) and x-axis is shown in Fig. 5, where both the electrode-axis (y) component σ_y and the transverse (x) component σ_x are negative. This compressive stress state is from the combined effect of thermal expansion and the electrode force [30,31]. The y-component is more compressive than the x-component ($\sigma_y < \sigma_x < 0$) for the entire duration of the RSW cycle. Under this biaxial stress state, the normal stress acting on a grain boundary inclined at angle θ to the y-axis is given by the standard plane-stress transformation [32]:

$$\sigma_n(\theta) = \sigma_y \cdot \sin^2(\theta) + \sigma_x \cdot \cos^2(\theta)$$

In the stress-assisted GB diffusion model, it is the stress gradient along the normal to the GB plane that governs the thermodynamic

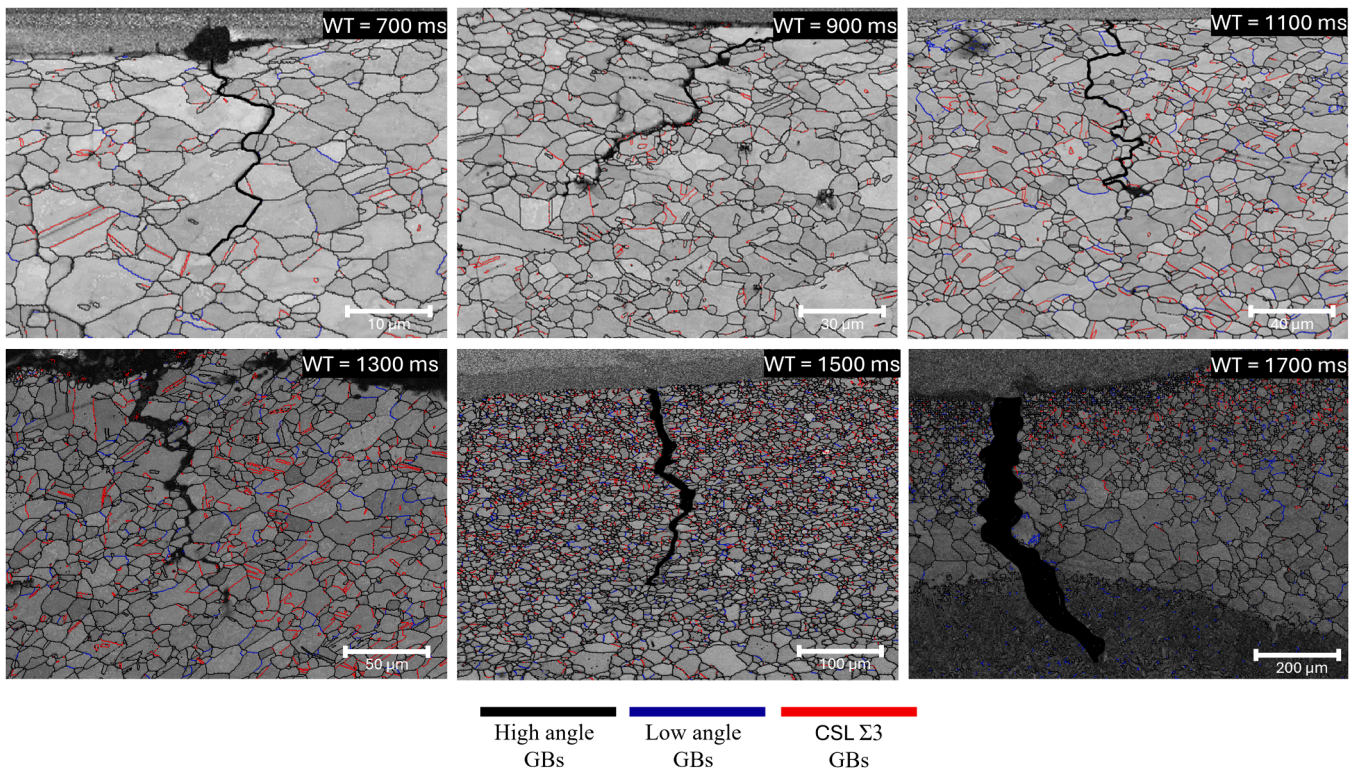


Fig. 2. EBSD image quality map showing LME cracks and grain structure for different RSW weld times.

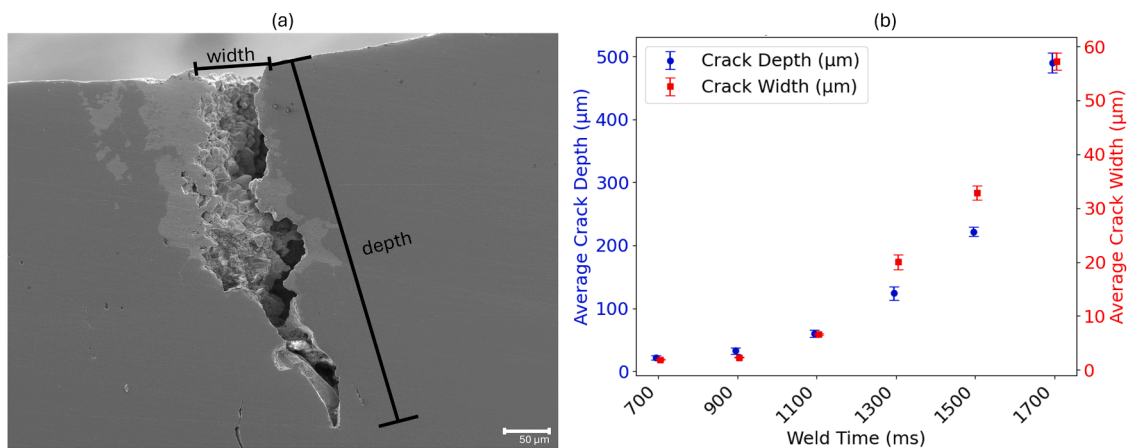


Fig. 3. (a) Schematic diagram for crack dimension measurement (b) Average LME crack depth and crack width at different weld times, with the error bars representing standard deviation.

driving force for Zn transport. The stress gradient causes a gradient in the chemical potential resulting in the thermodynamic driving force for diffusion [33]. The Fe-Zn system undergoes grain boundary wetting governed by the condition $\gamma_{GB} > 2\gamma_{SL}$ independent of the macroscopic stress state, where γ_{GB} is the surface energy of the grain boundary and γ_{SL} is the surface energy of the solid-liquid interface [34,35]. Once Zn has penetrated a boundary, the stress-assisted diffusion model predicts that the diffusing Zn atoms generate local tensile stress at the crack tip through a wedging mechanism, providing the driving force for intergranular decohesion even in the absence of macroscopic tensile loading [33]. The angle between an LME GB and the loading direction is denoted by θ , and the corresponding angle for an LME-free GB is denoted ϕ . From these angles, a stress factor is defined as the cosine of the angle the GB makes with the loading direction which is equal to 1 when the GB is parallel to the loading axis and 0 when the GB is perpendicular to the

loading axis. The stress factor therefore provides a normalised scalar measure of the mechanical driving force acting on each grain boundary. The macroscopic biaxial compressive field measured in this study therefore does not prevent LME from occurring. Boundaries experiencing the least compressive normal stress i.e. those most parallel to the electrode force direction, are the preferred pathways for Zn-driven crack propagation, which is the basis for the stress normalisation factor used in this analysis. It should be noted that the stress normalisation factor used throughout this analysis is a geometric approximation derived from the macroscopic, bulk stress field at the weld shoulder as computed by FEA. It does not capture the local stress state at individual GBs, which is modified by elastic and plastic anisotropy between neighbouring grains, local stress concentrations at triple junctions, and the changing temperature across the HAZ during the weld cycle [36]. As a result, the stress normalisation factor should be interpreted as a relative metric to

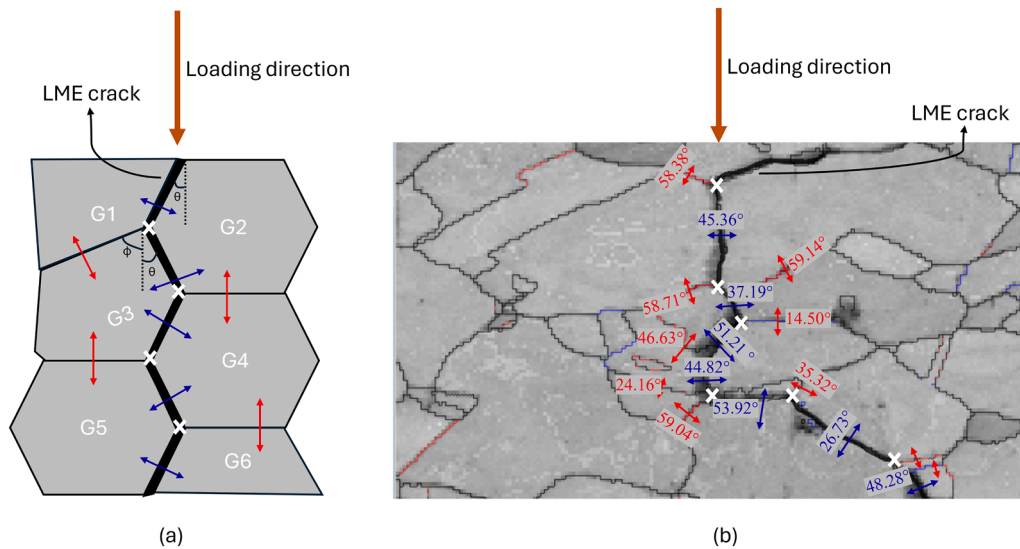


Fig. 4. (a) Schematic representation of grain structure surrounding LME crack with white X denoting GB triple junctions, blue arrows denoting misorientation between LME GBs and red arrows denoting LME-free GBs (b) Representative EBSD IQ map showing GB misorientation measurements surrounding LME cracks.

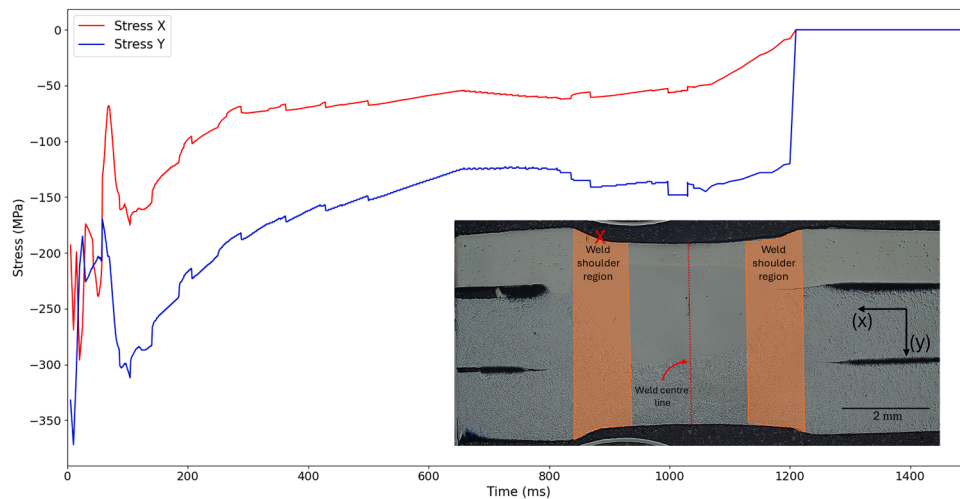


Fig. 5. Stress in the X and Y directions vs time plot in the weld shoulder region calculated using the FEA model at a weld time of 900 ms.

compare two competing boundaries at a triple junction. This approximation is considered acceptable to compare which of two boundaries at the same triple junction experiences the less compressive normal stress, where both boundaries are subject to the same macroscopic stress.

Fig. 4(b) shows a representative EBSD IQ map illustrating the LME crack path and the misorientation measurements made at LME GBs and

LME-free GBs at triple junctions ahead of the crack. The GB misorientations calculated from the EBSD data capture both the misorientation angle and the misorientation axis. This measurement procedure was applied to all LME cracks observed across the six weld times investigated in this study.

At a weld time of 1700 ms, the width of the LME crack was too large

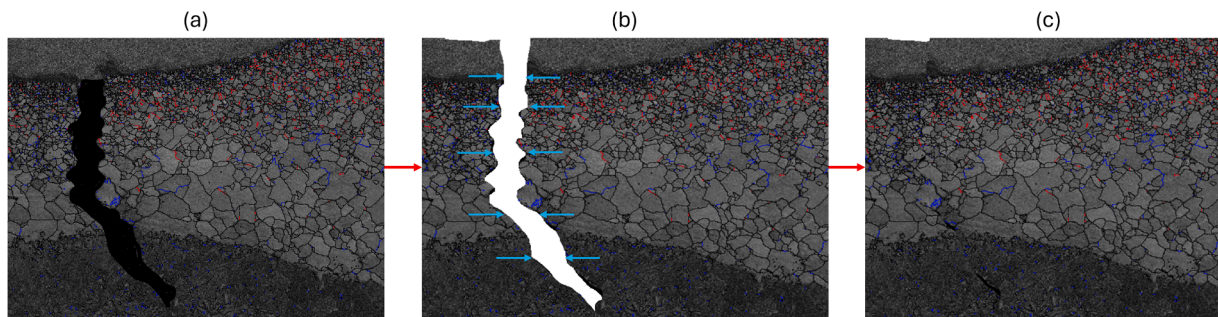


Fig. 6. (a) IQ map showing GBs at weld time = 1700 ms (b) process of 'closing' the LME crack to identify neighbouring grains (c) reconstructed grain boundary map to perform misorientation analysis.

to directly determine the original GB structure across the crack. To address this, the micrograph was separated along the crack and the regions on either side were reconstructed and stitched together, as illustrated in Fig. 6. This reconstruction was possible by matching features such as grain morphology and the geometry of the weld fusion zone on both sides of the crack, which allowed neighbouring grains to be identified. GB orientation relationships were determined only for the FCC TWIP phase of the steel and were not evaluated within the fusion zone.

3.3. GB misorientation and loading axis orientation

Fig. 7 presents the misorientation angle distributions for LME GBs and LME-free GBs for all weld times, and Fig. 8 shows the misorientation distribution function (MDF) map for LME and LME-free GBs combined in one map. The distribution of LME GB misorientation angles follows an approximately Gaussian profile centred in the range of 35-55°. This indicates that the LME crack does not exhibit a strong preference for a specific misorientation angle within in the HAGB range. The crack propagates through random HAGBs that constitutes the majority of boundaries in the material. The number of triple junctions identified for each weld time is summarised in Table 4. At each triple junction, there is an LME GB and LME-free GB ahead of it. From both Fig.s, it can be seen that for LME GBs, the MDF reveals a preferential clustering of misorientations in the $\langle 111 \rangle$ tilt axis family at misorientation angles between approximately 25° and 45° where the crack propagates through random HAGBs that constitutes the majority of boundaries in the material. In contrast, for LME-free GBs, the MDF displays a sharp, high-intensity peak at the $\langle 111 \rangle$ axis and misorientation angles of 55-65°, which corresponds to $\Sigma 3$ CSL coherent twin boundaries that are a characteristic microstructural feature of low stacking fault energy TWIP steels [10]. This observation holds consistently across all weld times investigated in this study: in every condition, the LME crack path never propagated through a $\Sigma 3$ twin boundary. The avoidance of $\Sigma 3$ boundaries by the LME crack, regardless of weld time or temperature indicates that these boundaries are a structural barrier to liquid metal penetration and crack propagation.

At each triple junction the LME crack passes through, the crack faces a choice between two GBs that differ in their misorientation angle and orientation relative to the loading axis. To determine which of these

factors govern the path the LME crack selects and how they are affected by weld time, the assessed misorientation and the stress normalisation factor is for both sets of GBs at each triple junction. Fig. 9 presents scatter plots of the stress normalisation factor against misorientation angle for LME GBs and LME-free GBs across all six weld times. GBs are classified into six categories to enable systematic comparison: (a) LME LAGBs (misorientation $< 15^\circ$), (b) LME HAGBs (misorientation $\geq 15^\circ$, non-CSL), (c) LME CSL GBs ($\Sigma 5$ - $\Sigma 41$, excluding $\Sigma 3$), (d) LME-free HAGBs, (e) LME-free CSL GBs ($\Sigma 5$ - $\Sigma 41$), and (f) LME-free $\Sigma 3$ GBs. For HAGBs through which the crack propagates (filled blue circles), the distribution evolves with weld time. At 700 ms, these boundaries are spread across the full stress normalisation factor range (~ 0.1 - 1.0) with misorientation angles between ~ 25 - 55° . With increasing weld time, the GBs progressively cluster at higher stress factors. When the weld time is above 1300 ms most points lie between 0.8-1.0, and at 1700 ms they are concentrated near 1. For LAGBs that the LME crack propagates through (filled blue triangles), the stress normalisation factor lies between 0.6 and 1.0 at all weld times, indicating that crack propagation through LAGBs occurs only when they are well aligned with the loading axis. $\Sigma 3$ CSL boundaries (filled red triangles) were consistently observed to be LME-free. Non- $\Sigma 3$ CSL GBs the LME crack propagated through (filled red squares) were not observed at the lowest weld time but appear at higher weld times, primarily at high stress normalisation factors, indicating crack propagation when their orientation is more aligned with the loading axis. LME-free HAGBs (unfilled blue circles) are distributed broadly across all stress factors and misorientation angles at every weld time, and this distribution does not change significantly between 700 ms and 1700 ms. However, their overall fraction decreases with weld time. LME-free non- $\Sigma 3$ CSL boundaries (filled red squares) are present across all stress factors up to a weld time of 1100 ms, but at higher weld times some of these boundaries allow LME cracks to propagate through when their stress factor is sufficiently high. The distribution of stress normalisation factors for LME and LME-free GBs and the average angle of both sets of GBs with the loading axis is shown in Fig. 10. These individual trends are further quantified in Fig. 13. For all weld times, the distribution for LME-free GBs remains largely unchanged across the full range of stress normalisation factors. In contrast, the distribution for LME GBs evolves with weld time. At 700 ms and 900 ms, although a peak is observed at high stress normalisation factors, LME GBs are

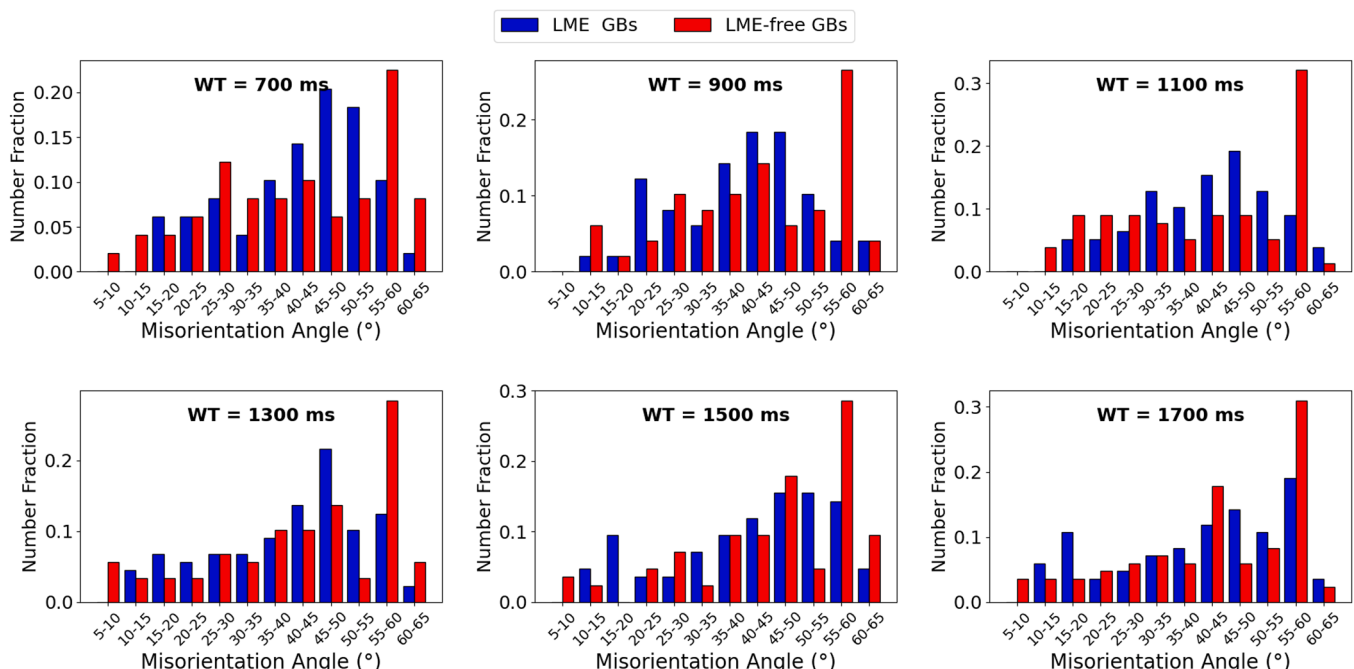


Fig. 7. Misorientation angle distribution of LME and LME-free GBs for all weld times.

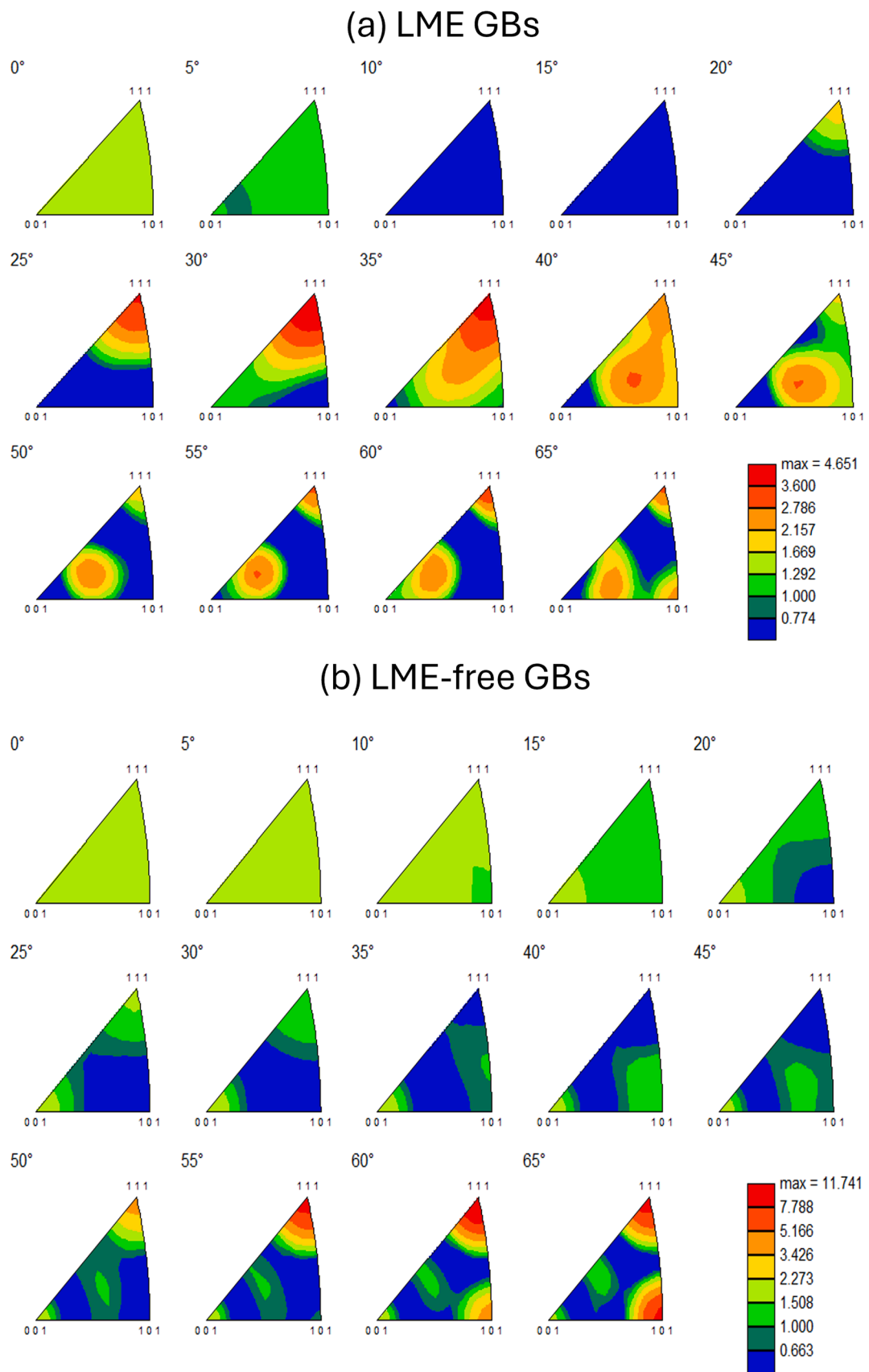


Fig. 8. Misorientation distribution function for (a) LME GBs (b) LME-free GBs.

Table 4
Number of triple junctions analysed at different weld times.

Weld time (ms)	Number of triple junctions analysed
700	52
900	55
1100	64
1300	77
1500	89
1700	85

present across the full range from 0 to 1. With increasing weld time, the fraction of LME GBs at higher stress normalisation factors (0.7-1.0) increases. By 1700 ms, no LME GBs are observed below a stress normalisation factor of 0.5, and approximately 80% of these GBs lie above 0.8.

Fig. 11(a) shows that the percentage of $\Sigma 3$ CSL boundaries remains approximately constant for all weld times. This is expected because these twin boundaries are uniformly distributed in the TWIP steel microstructure and are not affected by the welding parameters. Fig. 11 (b) shows the fraction of LME-free CSL boundaries that are not twin boundaries. This percentage decreases from ~26% at a weld time of 700

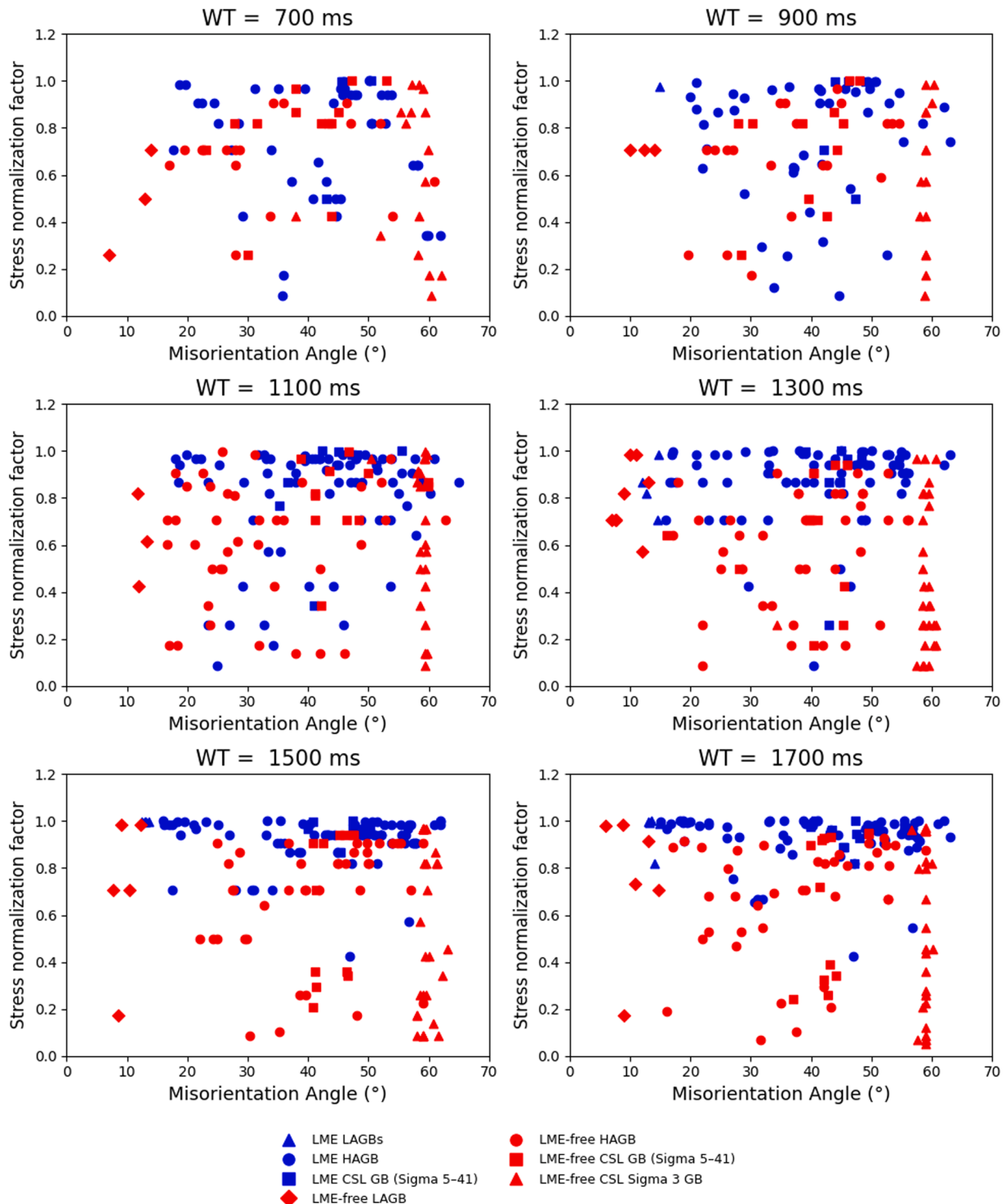


Fig. 9. GB misorientation angle vs stress normalisation factor with loading axis of different types of GBs for all weld times.

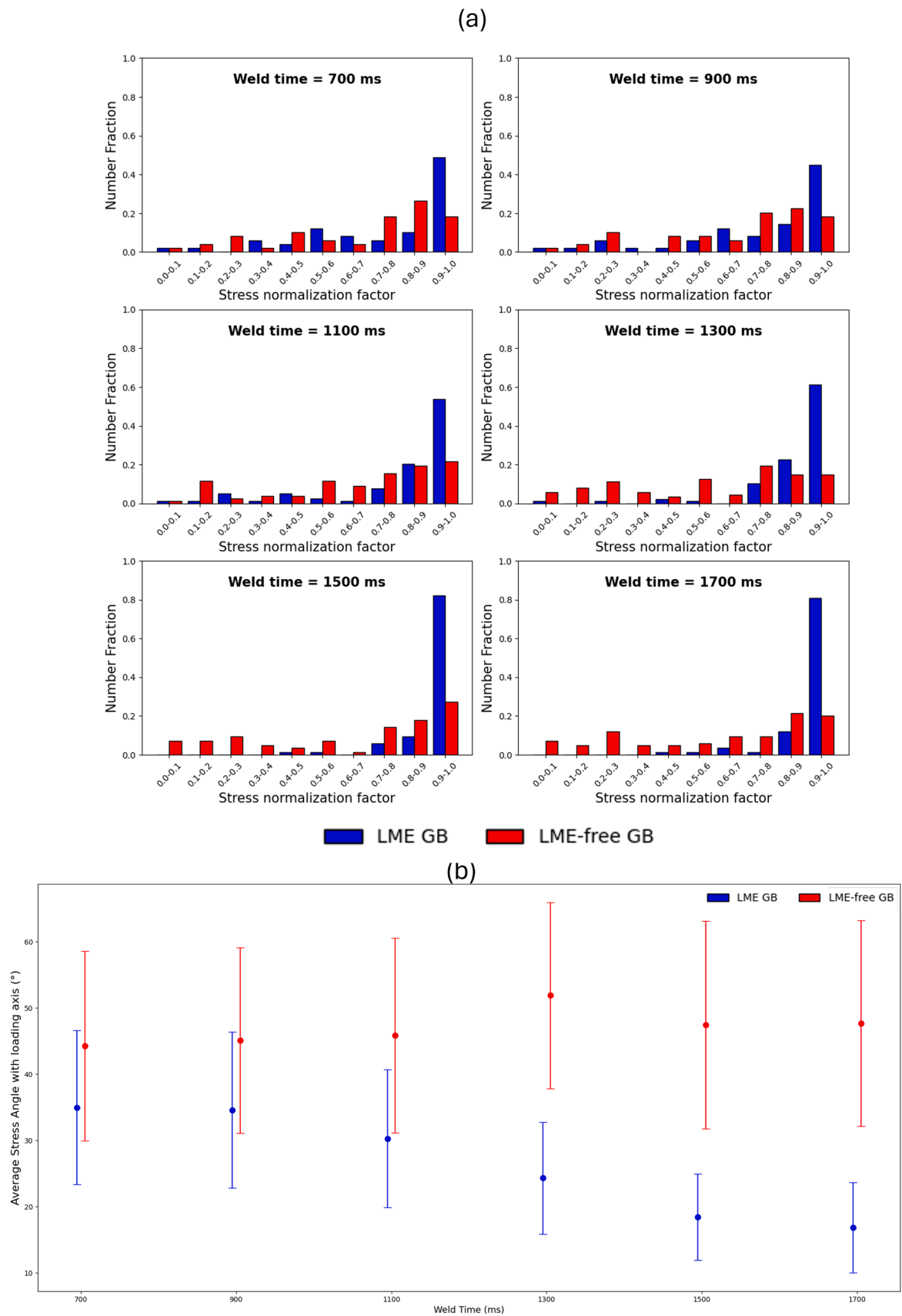


Fig. 10. (a) Distribution of the stress normalisation factor for LME and LME-free grains for weld times from 700 ms to 1700 ms (b) Average angle of LME and LME-free GBs with the loading axis for weld times from 700 ms to 1700 ms.

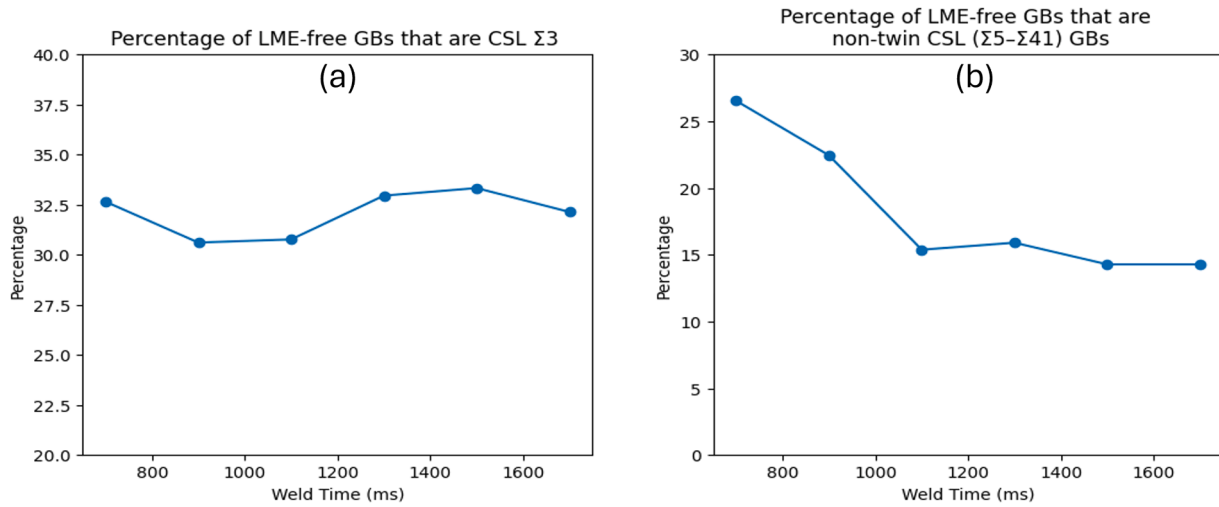


Fig. 11. For weld times between 700 ms and 1700 ms, (a) Percentage of LME-free GBs are not CSL $\Sigma 3$ twin GBs (b) percentage of LME-free CSL GBs that are non $\Sigma 3$.

ms to ~15% at 1700 ms. Since the overall GB distribution in the microstructure does not change with weld time, this indicates that a greater fraction of these boundaries are embrittled at higher weld times.

Fig. 12(a) shows the fraction of LME GBs that are LAGBs. This increases from ~6% at 700 ms to 17.4% at 1700 ms. Fig. 12(b) shows the percentage of LME GBs that are non-twin CSL boundaries ($\Sigma 5$ - $\Sigma 41$). This fraction is 2.6% at 700 ms, increases to ~4% at 1100 ms, and further increases to 16% at 1700 ms. When both boundaries ahead of a triple junction are random HAGBs, the preference for the boundary with the higher stress normalisation factor increases with weld time. At 700 ms, the boundary with the higher stress factor is selected in 63% of cases, increasing to 68% at 900 ms and 72% at 1100 ms. This trend becomes more pronounced at higher weld times, reaching 88% at 1300 ms, and remaining high at 85% and 87% for 1500 ms and 1700 ms, respectively.

Fig. 13(a) shows the percentage of triple junctions where the LME GB has a higher misorientation angle than the LME-free GB, excluding CSL boundaries. Previous studies indicate that GBs with higher misorientation angles are more susceptible to LME. At a weld time of 700 ms, the higher misorientation GB was the preferred crack path in 73% of the cases. This percentage is 68% at 900 ms and 72% at 1100 ms, but decreases to 58% at 1300 ms, 55% at 1500 ms, and 56% at 1700 ms, indicating a downward trend. Fig. 13(b) shows the percentage of cases where the LME GB has a higher stress normalisation factor than the LME-free GB, for non CSL boundaries. In contrast to misorientation, this

metric shows a clear increasing trend. At 700 ms, the boundary with the higher stress normalisation factor is the preferred crack path in 58% of the cases, increasing to 91% at 1700 ms.

4. Discussion

The results of this study are interpreted within the framework of stress assisted GB diffusion, which is the accepted transport mechanism for LME in the Fe-Zn system [16,20,37]. DiGiovanni et al. observed that Zn penetration depth increased with applied stress, with a diffusion profile predicted by the stress-assisted diffusion model of Klinger and Rabkin [20,33]. Murugan et al. showed that LME sensitivity in galvanized medium Mn steel during high-temperature tensile testing is governed not only by the presence of liquid Zn but by the fraction of effective liquid Zn available at the moment of deformation [38]. At the atomic scale, GB decohesion in the Fe-Zn system occurs when Zn atoms diffuse through the GB ahead of the propagating crack and weakens the Fe-Fe bonds and causes fracture under applied load [33]. Chen et al. found that the segregation of TWIP steel alloying elements like Al, Mn, Mo, and Ti to the α/γ interface has an effect on the interfacial cohesion [39]. Based on this framework, the results presented in the previous section are now examined in detail. The influence of GB misorientation and orientation with respect to the loading axis on LME crack propagation is discussed by considering each type of grain boundary

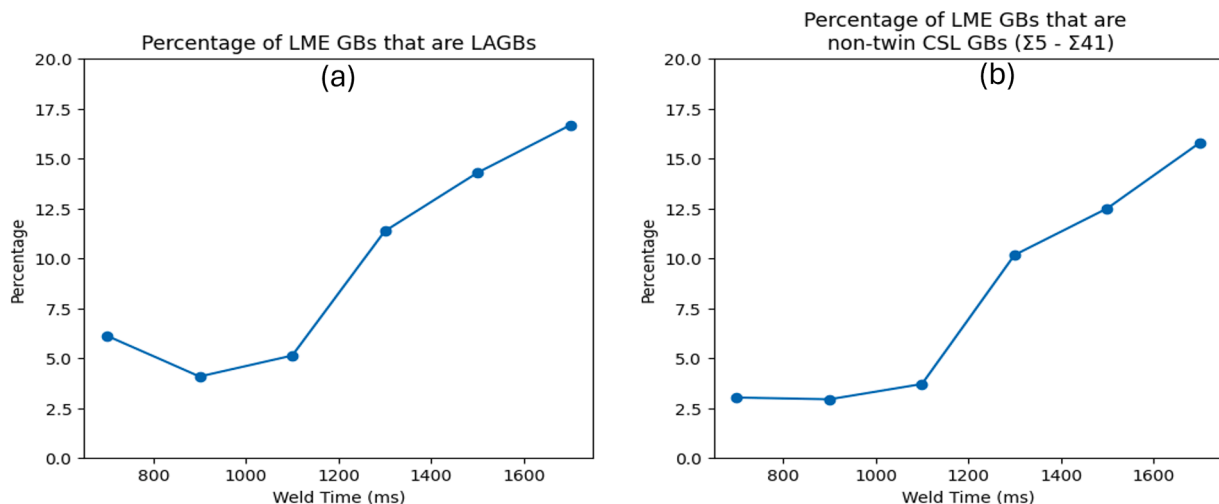


Fig. 12. For weld times between 700 ms and 1700 ms, (a) percentage of LME GBs that are LAGBs (b) percentage of LME GBs that are CSL $\Sigma 5$ to $\Sigma 41$.

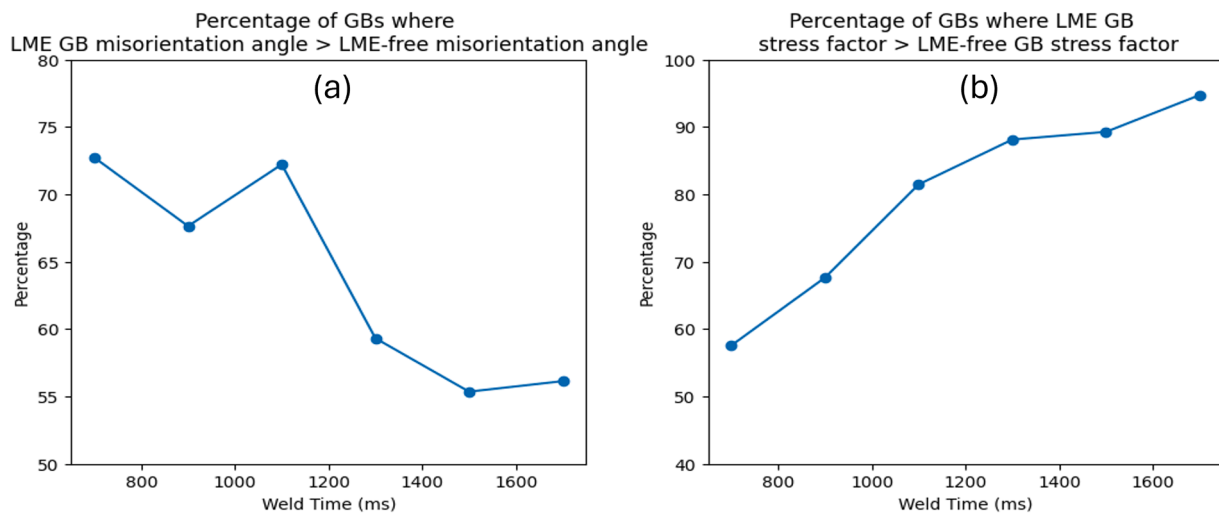


Fig. 13. For weld times between 700 ms and 1700 ms, (a) percentage of GBs where the LME GB misorientation angle is greater than the LME-free misorientation angle (b) percentage of GBs where the LME GB stress factor > LME-free GB stress factor.

individually. The analysis presented in this study is further used to propose a predictive index for LME susceptibility, combining the effects of grain boundary character and stress alignment. In addition, these results are used to identify grain boundary engineering strategies that can be applied to reduce LME susceptibility.

4.1. Effect of GB type on LME crack path

4.1.1. HAGBs

The misorientation angle distributions in Fig. 7 show that the LME crack propagates predominantly through random HAGBs, consistent with the general HAGB distribution of the recrystallised austenite in TWIP steel [40]. This observation is in agreement with the studies by Razmpoosh et al., Bertolo et al. and Bhattacharya et al. who noted that higher misorientation angles correspond to higher GB energy, greater excess free volume, and faster GB diffusivity for substitutional solutes, and makes stress-assisted Zn diffusion kinetically faster along these boundaries [20,24,27]. The MDF for LME GBs in Fig. 8 reveals clustering in the $\langle 111 \rangle$ tilt axis family at a misorientation of 25–45°, and is consistent with the observations of Bertolo et al. that misorientation angle above approximately 25° reduces the minimum stress factor required for LME to approach zero [27]. As more GBs become embrittled by Zn diffusion, the misorientation angle between competing boundaries at a triple junction becomes less useful in determining which boundary is susceptible to LME. When the analysis is limited to triple junctions where both competing boundaries are random HAGBs, the preference for the boundary with the higher stress normalisation factor increases with weld time. The percentage rises from 63% at 700 ms to 68% at 900 ms and 72% at 1100 ms, followed by a sharper increase to 88% at 1300 ms, and remains high at 85% and 87% for 1500 ms and 1700 ms, respectively. Since both boundaries in this case are structurally similar, this trend indicates that crack path selection is controlled by mechanical factors rather than GB misorientation. With increasing weld time, as more HAGBs become sufficiently embrittled, the crack preferentially follows boundaries better aligned with the loading axis.

4.1.2. CSL GBs

4.1.2.1. $\Sigma 3$ GBs. $\Sigma 3$ coherent twin boundaries are avoided by the LME crack for all six weld times, despite these boundaries constituting ~30–33% of available GBs. This observation validates previous findings by Razmpoosh et al and Bertolo et al. [24,27]. Bertolo et al. confirmed this resistance specifically in the same TWIP steel under Gleeble hot tensile

conditions, where no $\Sigma 3$ boundary participated in Zn penetration or cracking even at stress normalisation factors as high as 0.8 [22]. The present RSW study demonstrates that this was observed across a range of weld times and correspondingly high temperatures and weld heat inputs. The thermodynamic condition for liquid metal GB penetration requires $\gamma_{GB} > 2\gamma_{SL}$, where γ_{GB} is the grain boundary energy and γ_{SL} is the solid-liquid interfacial energy [23]. For coherent $\Sigma 3$ $\{111\}$ twin boundaries in FCC austenite, the near-zero excess free volume means this condition is not met under the conditions of RSW, independent of stress state. In Fig. 9, $\Sigma 3$ boundaries (filled green triangles) appear at stress normalisation factors between 0.8–1 in all weld time conditions, without the crack propagating at any weld time.

4.1.2.2. $\Sigma 5$ to $\Sigma 41$ CSL GBs. The fraction of non-twin CSL ($\Sigma 5$ – $\Sigma 41$) boundaries in LME-free GBs (Fig. 11a) varies from ~26% at 700 ms to ~15% at 1700 ms and the increase in LME GBs that are non-twin CSL boundaries (Fig. 11b) from ~3% to ~16% show that these GBs are more prevalent in the LME crack path as the weld time increases. At each weld time condition there is an effective diffusion depth for Zn governed by the combined effects of temperature, applied stress, and time. These CSL boundaries have a lower excess free volume and GB energy than random HAGBs but higher than $\Sigma 3$ [41]. Murugan et al. found that LME severity increases linearly with the fraction of effective liquid Zn at the deformation temperature [38]. In RSW, higher weld times increase peak HAZ temperature and reduce isothermal solidification extent during the weld cycle, increasing the effective liquid Zn fraction at the moment of peak tensile stress. In 100% of the observed cases where the LME crack traversed a non-twin CSL boundary, the stress factor of that boundary exceeded that of the competing LME-free GB at the same triple junction. Gong et al.'s observation also shows that GB decohesion under LME is dependent on orientation, with boundaries aligned parallel to the loading axis showing little or no cracking even when structurally susceptible [42]. This demonstrates that structural embrittlement is a necessary but not sufficient condition for non-twin CSL boundaries: the mechanical driving force must also be locally favourable.

4.1.3. LAGBs

LAGBs fraction increases with weld time in LME GBs from approximately 6% at 700 ms to ~17% at 1700 ms (Fig. 12a). In contrast to random HAGBs, which at a weld time of 700 ms are distributed across a wide range of stress normalisation factors, LAGBs appear in the crack path exclusively at stress normalisation factors above 0.7 across all weld times. Razmpoosh et al. confirmed that low-angle random boundaries

resist LME [24], and Bertolo et al. found in the same TWIP steel that LAGBs required a normalised stress factor of at least 0.5 to participate in LME under hot tensile conditions [27]. The present RSW results are consistent with both findings, and show that LAGBs are only affected by LME when they are well-aligned with the loading axis, when the stress normalisation factor is above 0.5. At weld times below 1300 ms, Zn diffusion is insufficient to overcome the barrier for diffusion via LAGBs [21,43]. As weld time increases and HAZ temperatures rise, the Zn diffusivity along all boundary types increases, and the greater cumulative Zn flux eventually reaches the threshold required to embrittle even LAGBs [17,33]. In every observed case where the LME crack traversed a LAGB, the stress normalisation factor of that LAGB exceeded that of the competing boundary at the same triple junction. At 700, 900 and 1100 ms, the differences in the percentage of LME GBs that are LAGBs are within ~2% of each other. Thus it is not possible to determine with confidence whether this apparent reduction reflects a real physical trend or statistical scatter.

4.2. Misorientation angle vs stress normalisation factor

Fig. 13 shows that the preference for the higher-misorientation boundary declines from 73% at 700 ms to 56% at 1700 ms, while the preference for the boundary with the higher stress normalisation factor increases from 58% to 93% over the weld time same range. The stress-assisted diffusion model of Klinger and Rabkin predicts that the diffusion flux along a grain boundary scales with both the GB diffusivity and the normal stress acting on the boundary [33]. The GB diffusivity itself is an exponential function of GB energy, which in the HAGB regime is controlled principally by the excess free volume associated with the GB structure [20,21]. At lower temperatures, the absolute GB diffusivity is lower across all GB types, and the relative difference in diffusivity between a high-energy and a lower-energy random HAGB is large enough to make misorientation a criteria that determines the crack path. A GB with a higher misorientation angle presents a structurally more open pathway for Zn penetration, such that the crack preferentially selects it even when the stress alignment is less favourable. This is consistent with the observation of Razmpoosh et al. that crack propagation in the Fe-Zn system is a function of both misorientation angle and the stress component perpendicular to the boundary plane, with misorientation acting as a necessary condition for penetration at low applied stress [23].

As weld time increases, peak HAZ temperatures rises. Mahadevan et al. showed in this same TWIP steel system that Zn diffusion distance ahead of LME cracks increases with weld time, with GB diffusion estimated to be approximately 30 times greater than bulk diffusion [19]. As temperature increases, the relative differences in diffusivity between competing random HAGBs of different misorientation angle narrow, because all boundaries in the HAGB regime share a qualitatively similar open atomic structure. The misorientation dependent difference that made one boundary a more preferred crack path than another at low weld times becomes less of a deciding factor when both boundaries are now above the diffusion threshold required for Zn penetration and intergranular decohesion.

Murugan et al. demonstrated that LME severity scales with the fraction of effective liquid Zn present at the moment of peak tensile stress [38]. At higher weld times, the effective Zn fraction available at the weld shoulder increases. Once both competing boundaries at a triple junction are susceptible to Zn penetration, the mechanical driving force becomes the sole remaining discriminator. Boundaries more parallel to the loading axis experience a less compressive (or more tensile) normal stress, which both thermodynamically favours GB wetting per the condition $\gamma_{GB} > 2\gamma_{SL}$ and increases the stress-assisted Zn flux through the wedging mechanism described by Klinger and Rabkin [33,34]. Gong et al. similarly observed that once a critical stress threshold is exceeded, the orientation of the boundary relative to the applied stress axis controls the depth and rate of liquid metal penetration (angle θ), with

boundaries parallel to the loading axis being least mechanically suppressed [25]. The two factors should therefore be understood not as competing explanations for LME crack path selection, but as sequential governing parameters whose relative effects shifts as the temperature of the process increases. The key novel finding of this study is therefore that the relative importance of GB orientation with the stress axis increases with weld time and temperature. At lower weld times, GB misorientation has a greater influence on crack path selection, while at higher weld times the orientation of the boundary relative to the stress axis becomes progressively more important. This has not previously been identified or quantified under RSW conditions.

4.3. Proposed framework for LME GB susceptibility index

The trends identified above provide the basis for an LME susceptibility index. Such an index, combining GB energy, stress normalisation factor, and Zn diffusivity, offers a framework for assessing which boundaries are more likely to be LME susceptible under a given set of conditions. This could be a predictive tool for grain boundary engineering strategies aimed at reducing LME in RSW of TWIP steel.

The GB structural character is a function of five independent macroscopic degrees of freedom: three parameters describing the crystallographic misorientation between adjacent grains, and two parameters describing the inclination of the boundary plane [44]. The present analysis captures the misorientation component through the misorientation axis-angle pair, and approximates the mechanical component through the angle relative to the loading direction. Both are projections of higher-dimensional quantities, which cannot directly be used to predict LME. The Read-Shockley model gives the GB energy $\gamma \propto \theta(A - \ln \theta)$, where A is a material constant that depends on elastic moduli and Burgers vector [44]. This function increases with θ up to approximately 15°, where the dislocation cores begin to overlap and the model breaks down. In the HAGB regime, GB energy no longer varies with misorientation angle alone and is also dependent on the misorientation axis. The depth and width of the energy minima at CSL orientations depend on the Σ value and the boundary plane orientation. For $\Sigma 3$ coherent twin boundaries on the (111) plane, the energy approaches zero for perfectly coherent boundaries [44]. This has also been experimentally verified in Cu bicrystals by Wang et al [45]. Saylor et al. confirmed experimentally that the GB energy function shows Read-Shockley behaviour at small misorientations and a broad minimum near the $\Sigma 3$ misorientation, and additionally found that the energy depends on the rotation axis [46]. The trends observed across all weld times and boundary types suggest that a unified predictive criterion for crack path selection at a triple junction is a useful direction for future work. Based on the present observations, such an index would need to incorporate at minimum: (i) the GB energy as a proxy for structural susceptibility to Zn penetration; (ii) a temperature-dependent Zn diffusivity term that scales with the excess free volume; and (iii) a mechanical stress normalisation factor capturing boundary alignment with the loading axis. The present study does not develop or validate such an index quantitatively; rather, it is proposed as a framework to guide future experimental and modelling efforts, informed by the trends identified here.

Several limitations would need to be acknowledged in applying such an index. The GB energy required as input is not measured for this specific TWIP steel HAZ microstructure and would need to be determined experimentally through five-parameter characterisation or atomistic simulation. Additionally, the relationship between GB energy and Zn diffusivity is taken from an empirical approximation that has been validated primarily in other FCC systems rather than Fe-Zn-Mn at RSW temperatures, and the relevant diffusion constants are not accurately calculated for the conditions studied here. The stress normalisation factor used throughout this study is a static approximation of what is in reality a transient, spatially varying stress tensor that evolves throughout the weld cycle [20]. Finally, the framework does not incorporate grain boundary chemistry, which Razmpoosh et al. showed

can independently modify embrittlement susceptibility through solute segregation [24]. Validating such an index quantitatively would require five-parameter GB characterisation to resolve boundary plane orientation, atom probe or STEM-EDS measurements of solute segregation at individual boundaries, and stress state calculations at individual GBs from crystal plasticity modelling rather than the macroscopic FEA stress field used in this study.

4.4. Grain boundary engineering for LME mitigation

The results of this study show that grain boundary engineering (GBE) is a potential strategy to reduce LME susceptibility in TWIP steel. Across all six weld times investigated, $\Sigma 3$ coherent twin boundaries were avoided by the LME crack, regardless of their orientation relative to the loading axis. This behaviour establishes that the structural resistance of $\Sigma 3$ boundaries to liquid Zn penetration is not overcome by the mechanical driving force alone. Their near-zero excess free volume prevents the thermodynamic condition $\gamma_{GB} > 2\gamma_{SL}$ required for GB wetting from being satisfied under RSW conditions. The finding that non- $\Sigma 3$ CSL boundaries ($\Sigma 5$ - $\Sigma 41$) similarly resisted LME at lower weld times, only becoming relevant at higher weld times at high stress normalisation factors, indicating that CSL GBs also offer a degree of structural protection.

GBE through thermomechanical processing (TMP) can be used to increase the fraction of low- Σ CSL boundaries through repeated cycles of small plastic pre-strain and subsequent annealing [47]. TMP drives strain-induced grain boundary migration (SIBM) accompanied by annealing twin formation, which creates CSL boundaries and disrupts the connected random HAGB network [48]. Kokawa et al. demonstrated that an optimised TMP treatment in type 304 austenitic stainless steel maximises the CSL boundary fraction and produces a clear discontinuity in the corrosive random boundary network, arresting the propagation of intergranular attack from the surface [49]. Zhang et al. applied 5% compressive pre-strain to 316L austenitic stainless steel and showed that the special boundary fraction increased from 55% to 74% after annealing at 1273 K for 90 minutes, with the growing $\Sigma 9$ and $\Sigma 27$ boundary populations progressively replacing segments of the random HAGB network [50]. An LME crack cannot propagate indefinitely if the random boundary network is interrupted by clusters of CSL boundaries that are structurally impermeable to liquid Zn.

The present study demonstrates that the relative influence of GB misorientation on crack path selection reduces with increasing weld time: at 700 ms, higher misorientation boundaries are preferred in 73% of triple junctions, but falls to 56% at 1700 ms. At the highest weld times and heat inputs, the combination of temperature, Zn availability, and increased peak stresses at the weld periphery means that even non- $\Sigma 3$ CSL boundaries become susceptible to LME. Practically, a GBE treatment would need to be integrated as a final heat treatment step after the conventional continuous annealing cycle, or designed as a modified annealing schedule compatible with galvanising operations, since standard continuous annealing produces a largely recrystallised microstructure. The LME susceptibility index framework proposed in the preceding section, which would incorporate GB energy, stress normalisation factor, and a temperature-dependent diffusivity term, could serve as a quantitative design target for such a process.

5. Conclusions

This study investigated the influence of GB misorientation and orientation relative to the loading axis on LME crack path in Zn-coated TWIP steel RSW across six weld times from 700 ms to 1700 ms. The following conclusions can be drawn:

- LME GBs were predominantly random HAGBs with misorientation angles of 35-55°. $\Sigma 3$ coherent twin boundaries were LME-free at every weld time investigated regardless of their orientation relative

to the loading axis. Non-twin CSL boundaries ($\Sigma 5$ - $\Sigma 41$) were predominantly LME-free at low weld times but progressively became LME GBs at higher weld times, at high stress normalisation factors and only when their stress factor exceeded that of the competing LME-free GB at the same triple junction.

- The fraction of triple junctions at which the LME GB had a higher stress normalisation factor than the competing LME-free GB increased from 58% at 700 ms to 91% at 1700 ms. Simultaneously, the preference for the higher misorientation GB reduced from 73% to 56%. LAGBs appeared as LME GBs only at high weld times and only at high stress normalisation factors.
- An LME GB susceptibility index is proposed that combines GB orientation and character, stress-assisted diffusion and a mechanical orientation factor. This framework provides a basis for interpreting the observed trends across all boundary types and weld times within a single predictive criterion, and could be a quantitative design target for grain boundary engineering strategies aimed at reducing LME susceptibility in TWIP steel during RSW.

Data availability

The data is part of an ongoing study and can be shared upon request.

Funding

This publication is part of the project N19010 in the Partnership Program of the Materials Innovation Institute M2i framework, which is partly financed by the Dutch Research Council (NWO) and the partners Tata Steel and AutomotiveNL.

CRediT authorship contribution statement

Gautham Mahadevan: Writing – original draft, Visualization, Validation, Methodology, Investigation, Formal analysis, Data curation, Conceptualization. **Soheil Sabooni:** Writing – review & editing, Validation, Methodology, Conceptualization. **Vera Popovich:** Writing – review & editing, Validation, Supervision, Conceptualization. **Leo A.I. Kestens:** Writing – review & editing, Supervision, Methodology, Conceptualization. **Marcel Hermans:** Writing – review & editing, Supervision, Methodology, Conceptualization.

Declaration competing interest

The authors declare that they have no known competing financial interests or personal relationships that could have appeared to influence the work reported in this paper.

Acknowledgments

We acknowledge Kees Kwakernaak from TU Delft for the help with the use of the SEM and EBSD equipment. We would like to thank He Gao from Tata Steel Netherlands for his assistance with SORPAS, and the Welding and Joining Knowledge Group at Tata Steel Netherlands for providing the facilities to perform RSW tests.

References

- [1] A. Candela, G. Sandrini, M. Gadola, D. Chindamo, P. Magri, Lightweighting in the automotive industry as a measure for energy efficiency: review of the main materials and methods, *Heliyon* 10 (2024) e29728, <https://doi.org/10.1016/j.heliyon.2024.e29728>.
- [2] J.E. Norkett, M.D. Dickey, V.M. Miller, A review of liquid metal embrittlement: cracking open the disparate mechanisms, *Metall. Mater. Trans. A* 52 (2021) 2158–2172, <https://doi.org/10.1007/s11661-021-06256-y>.
- [3] T.B. Hilditch, T. de Souza, P.D. Hodgson, 2 - Properties and automotive applications of advanced high-strength steels (AHSS), in: M. Shome, M. Tumuluru (Eds.), *Weld Join Adv High Strength Steels AHSS* [Internet], Woodhead Publishing, 2015,

- pp. 9–28, <https://doi.org/10.1016/B978-0-85709-436-0.00002-3> [cited 2022 July 6].
- [4] R. Kuziak, R. Kawalla, S. Waengler, Advanced high strength steels for automotive industry, *Arch. Civ. Mech. Eng.* 8 (2008) 103–117, [https://doi.org/10.1016/S1644-9665\(12\)60197-6](https://doi.org/10.1016/S1644-9665(12)60197-6).
- [5] Demeri M. Advanced High-Strength Steels: Science, Technology, and applications - ASM international [Internet]. [cited 2022 June 16]. https://www.asminternational.org/bestsellers/-/journal_content/56/10192/05370G/PUBLICATION. Accessed 16 June 2022.
- [6] H. Zhang, J. Senkara, Resistance Welding: Fundamentals and Applications, CRC Press, Boca Raton, 2005, <https://doi.org/10.1201/b12507>.
- [7] D. Bhattacharya, Liquid metal embrittlement during resistance spot welding of Zn-coated high-strength steels, *Mater. Sci. Technol.* Taylor Francis; 34 (2018) 1809–1829, <https://doi.org/10.1080/02670836.2018.1461595>.
- [8] J. Barthelme, A. Schram, V. Wesling, Liquid metal embrittlement in resistance spot welding and hot tensile tests of surface-refined TWIP steels, in: *IOP Conf Ser Mater Sci Eng* 118, 2016 012002, <https://doi.org/10.1088/1757-899X/118/1/012002>.
- [9] H. Kang, L. Cho, C. Lee, B.C. De Cooman, Zn Penetration in Liquid Metal Embrittled TWIP Steel, *Metall. Mater. Trans. A* 47 (2016) 2885–2905, <https://doi.org/10.1007/s11661-016-3475-x>.
- [10] C. Béal, Mechanical behaviour of a new automotive high manganese TWIP steel in the presence of liquid zinc [Internet] [Theses], INSA de Lyon, <https://tel.archives-ouvertes.fr/tel-00679521>, 2011. Accessed 9 Aug 2022.
- [11] S-H Hong, J-H Kang, D. Kim, S-J. Kim, Si effect on Zn-assisted liquid metal embrittlement in Zn-coated TWIP steels: importance of Fe-Zn alloying reaction, *Surf. Coat. Technol.* 393 (2020) 125809, <https://doi.org/10.1016/j.surfcoat.2020.125809>.
- [12] D. Bhattacharya, L. Cho, J. Colburn, D. Smith, D. Marshall, E. van der Aa, et al., Influence of selected alloying variations on liquid metal embrittlement susceptibility of quenched and partitioned steels, *Mater. Des.* 224 (2022) 111356, <https://doi.org/10.1016/j.matdes.2022.111356>.
- [13] W. Dong, H. Pan, M. Lei, K. Ding, Y. Gao, Zn penetration and its coupled interaction with the grain boundary during the resistance spot welding of the QP980 steel, *Scr. Mater.* 218 (2022) 114832, <https://doi.org/10.1016/j.scriptamat.2022.114832>.
- [14] S.P. Murugan, K. Mahmud, C. Ji, I. Jo, Y-D Park, Critical design parameters of the electrode for liquid metal embrittlement cracking in resistance spot welding, *Weld World* 63 (2019) 1613–1632, <https://doi.org/10.1007/s40194-019-00797-y>.
- [15] D-Y Choi, A. Sharma, S-H Uhm, J.P. Jung, Liquid metal embrittlement of resistance spot welded 1180 TRIP steel: effect of electrode force on cracking behavior, *Met. Mater. Int.* 25 (2019) 219–228, <https://doi.org/10.1007/s12540-018-0180-x>.
- [16] E.E. Glickman, Grain boundary grooving accelerated by local plasticity as a possible mechanism of liquid metal embrittlement, *Interface Sci.* 11 (2003) 451–459, <https://doi.org/10.1023/A:1026100112248>.
- [17] E.E. Glickman, Dissolution condensation mechanism of stress corrosion cracking in liquid metals: driving force and crack kinetics, *Metall. Mater. Trans. A* 42 (2011) 250–266, <https://doi.org/10.1007/s11661-010-0429-6>.
- [18] V.V. Popovich, I.G. Dmukhovskaya, Rebinder effect in the fracture of armco iron in liquid metals, *Sov. Mater. Sci. Transl. Fiz-Khimicheskaya Mekhanika Mater. Acad. Sci. Ukr SSR* 14 (1979) 365–370, <https://doi.org/10.1007/BF01154711>.
- [19] Mahadevan G, Bertolo V, Sabooni S, Popovich V, Kestens LAI, Hermans M. Characterizing zinc diffusion during liquid metal embrittlement of resistance spot welded TWIP steel. *Weld World*. 2026; <https://doi.org/10.1007/s40194-026-02384-4>.
- [20] C. DiGiovanni, A. Ghatei Kalashami, E. Biro, N.Y. Zhou, Liquid metal embrittlement transport mechanism in the Fe/Zn system: stress-assisted diffusion, *Mater. (Oxf)* 18 (2021) 101153, <https://doi.org/10.1016/j.mta.2021.101153>.
- [21] Y. Hao, C. Tan, X. Yu, R. Chen, Z. Nie, Y. Ren, et al., Effect of grain boundary misorientation angle on diffusion behavior in molybdenum-tungsten systems, *J. Alloys. Compd.* 819 (2020) 152975, <https://doi.org/10.1016/j.jallcom.2019.152975>.
- [22] D. Bhattacharya, L. Cho, E. van der Aa, A. Pichler, N. Pottore, H. Ghassemi-Armaki, et al., Influence of the starting microstructure of an advanced high strength steel on the characteristics of Zn-assisted liquid metal embrittlement, *Mater. Sci. Eng. A* 804 (2021) 140391, <https://doi.org/10.1016/j.msea.2020.140391>.
- [23] M.H. Razmpoosh, C. DiGiovanni, Y.N. Zhou, E. Biro, Pathway to understand liquid metal embrittlement (LME) in Fe-Zn couple: from fundamentals toward application, *Prog. Mater. Sci.* 121 (2021) 100798, <https://doi.org/10.1016/j.pmatsci.2021.100798>.
- [24] M.H. Razmpoosh, A. Macwan, F. Goodwin, E. Biro, Y. Zhou, Role of random and coincidence site lattice grain boundaries in liquid metal embrittlement of iron (FCC)-Zn couple, *Metall. Mater. Trans. A* 51 (2020) 3938–3944, <https://doi.org/10.1007/s11661-020-05857-3>.
- [25] X. Gong, F. Hu, J. Chen, H. Wang, H. Gong, J. Xiao, et al., Effect of temperature on liquid metal embrittlement susceptibility of a Fe10Cr4Al ferritic alloy in contact with stagnant lead-bismuth eutectic, *J. Nucl. Mater.* 537 (2020) 152196, <https://doi.org/10.1016/j.jnucmat.2020.152196>.
- [26] S-H Hong, D-R Eo, S. Lee, J-W Cho, S-J. Kim, Strong resistance to Zn-assisted liquid metal embrittlement of austenitic-TWIP/martensitic-HSLA multi-layered steel sheets additively manufactured by laser cladding, *Acta Mater.* 258 (2023) 119224, <https://doi.org/10.1016/j.actamat.2023.119224>.
- [27] V. Bertolo, G. Mahadevan, R.H. Petrov, V. Popovich, The role of microstructure in crack growth during liquid metal embrittlement of Zn-galvanized TWIP steel, *J. Mater. Res. Technol.* 38 (2025) 2569–2577, <https://doi.org/10.1016/j.jmrt.2025.08.097>.
- [28] V. Bertolo, G. Mahadevan, R. de Kloe, R.H. Petrov, V. Popovich, Decoupling early-stage cracking and propagation mechanisms in liquid metal embrittlement of Zn-galvanized TWIP steel, *J. Mater. Res. Technol.* 38 (2025) 1617–1632, <https://doi.org/10.1016/j.jmrt.2025.08.055>.
- [29] Z. Ling, M. Wang, L. Kong, K. Chen, Towards an explanation of liquid metal embrittlement cracking in resistance spot welding of dissimilar steels, *Mater. Des.* 195 (2020) 109055, <https://doi.org/10.1016/j.matdes.2020.109055>.
- [30] X. Wan, Y. Wang, P. Zhang, Numerical simulation on deformation and stress variation in resistance spot welding of dual-phase steel, *Int. J. Adv. Manuf. Technol.* 92 (2017) 2619–2629, <https://doi.org/10.1007/s00170-017-0191-7>.
- [31] S.P. Murugan, V. Vijayan, C. Ji, Y.D. Park, Four types of LME cracks in RSW of Zn-coated AHSS, *Weld. J.* 99 (2020) 75s–92s.
- [32] S.P. Timoshenko, J.N. Goodier, H.N. Abramson, Theory of elasticity (3rd ed.), *J. Appl. Mech.* 37 (1970) 888, <https://doi.org/10.1115/1.3408648>.
- [33] L. Klinger, E. Rabkin, The effect of stress on grain boundary interdiffusion in a semi-infinite bicrystal, *Acta Mater.* 55 (2007) 4689–4698, <https://doi.org/10.1016/j.actamat.2007.04.039>.
- [34] T. Auger, L.L. Wang, D.D. Johnson, X. Gong, First-principles study of grain-boundary wetting in Fe-Σ5(013)[100] tilt boundary, *Acta Mater.* 265 (2024) 119635, <https://doi.org/10.1016/j.actamat.2023.119635>.
- [35] M. Arndt, P. Kürsteiner, T. Truglas, J. Duchoslav, K. Hingerl, D. Stifter, et al., Multiscale Investigation of Microcracks and Grain Boundary Wetting in Press-Hardened Galvanized 20MnB8 Steel, *Metals*, 14, Multidisciplinary Digital Publishing Institute, 2023, <https://doi.org/10.3390/met14010046> [cited 2026 Mar 24].
- [36] C. Zheng, L. Xu, X. Feng, Q. Huang, Y. Li, Z. Zhang, et al., Influence of Grain Orientation and Grain Boundary Features on Local Stress State of Cu-8Al-11Mn Alloy Investigated Using Crystal Plasticity Finite Element Method, 15, Multidisciplinary Digital Publishing Institute, 2022, <https://doi.org/10.3390/ma15196950>. Materials [cited 2026 Mar 25].
- [37] J-U Kim, S.P. Murugan, J-S Kim, W. Yook, C-Y Lee, C. Ji, et al., Liquid metal embrittlement during the resistance spot welding of galvanized steels: synergy of liquid Zn, α-Fe(Zn) and tensile stress, *Sci. Technol. Weld Join* 26 (2021) 196–204, <https://doi.org/10.1080/13621718.2021.1880816>. SAGE Publications.
- [38] S.P. Murugan, J. Kim, J. Kim, Y. Wan, C. Lee, J.B. Jeon, et al., Role of liquid Zn and α-Fe(Zn) on liquid metal embrittlement of medium Mn steel: an ex-situ microstructural analysis of galvanized coating during high temperature tensile test, *Surf. Coat. Technol.* 398 (2020) 126069, <https://doi.org/10.1016/j.surfcoat.2020.126069>.
- [39] L. Chen, Y. Zhao, X. Qin, Some aspects of high manganese twinning-induced plasticity (TWIP) steel, a review, *Acta Metall. Sin. Engl. Lett.* 26 (2013) 1–15, <https://doi.org/10.1007/s40195-012-0501-x>.
- [40] C. Beal, X. Kleber, D. Fabregue, M. Bouzekri, Embrittlement of a zinc coated high manganese TWIP steel, *Mater. Sci. Eng. A* 543 (2012) 76–83, <https://doi.org/10.1016/j.msea.2012.02.049>.
- [41] H. Beladi, G.S. Rohrer, The distribution of grain boundary planes in interstitial free steel, *Metall. Mater. Trans. A* 44 (2013) 115–124, <https://doi.org/10.1007/s11661-012-1393-0>.
- [42] X. Gong, P. Marmy, A. Volodin, B. Amin-Ahmadi, L. Qin, D. Schryvers, et al., Multiscale investigation of quasi-brittle fracture characteristics in a 9Cr–1Mo ferritic–martensitic steel embrittled by liquid lead–bismuth under low cycle fatigue, *Corros. Sci.* 102 (2016) 137–152, <https://doi.org/10.1016/j.corsci.2015.10.003>.
- [43] K-D Bauer, M. Todorova, K. Hingerl, J. Neugebauer, A first principles investigation of zinc induced embrittlement at grain boundaries in bcc iron, *Acta Mater.* 90 (2015) 69–76, <https://doi.org/10.1016/j.actamat.2015.02.018>.
- [44] Humphreys, Hatherley. The structure and energy of grain boundaries [Internet]. [cited 2026 Mar 18]. <https://doi.org/10.1016/B978-008044164-1/50008-6>.
- [45] J. Wang, N. Li, A. Misra, Structure and stability of Σ3 grain boundaries in face centered cubic metals, *Philos. Mag. Taylor Francis*; 93 (2013) 315–327, <https://doi.org/10.1080/14786435.2012.716908>.
- [46] D.M Saylor, A. Morawiec, B.L Adams, G.S. Rohrer, Misorientation dependence of the grain boundary energy in magnesia, *Interface Sci.* 8 (2000) 131–140, <https://doi.org/10.1023/A:1008764219575>.
- [47] C. Takushima, J. Hamada, S. Tsurekawa, Rapid achievement of high frequency of CSL boundaries in austenitic stainless steel via reduced stacking fault energy, *ISIJ Int.* 65 (2025) 133–141, <https://doi.org/10.2355/isijinternational.ISIJINT-2024-259>.
- [48] F. Shi, X. Li, Y. Hu, C. Su, C. Liu, Optimization of grain boundary character distribution in Fe-18Cr-18Mn-0.63N high-nitrogen austenitic stainless steel, *Acta Metall. Sin. Engl. Lett.* 26 (2013) 497–502, <https://doi.org/10.1007/s40195-013-0323-5>.
- [49] H. Kokawa, M. Shimada, Z.J. Wang, Y.S. Sato, M. Michiuchi, Grain boundary engineering for intergranular corrosion resistant austenitic stainless steel, *Key. Eng. Mater. Trans. Tech. Public. Ltd* 261–263 (2004) 1005–1010, <https://doi.org/10.4028/www.scientific.net/KEM.261-263.1005>.
- [50] M. Zhang, C. Zhang, H. Wu, B. Yang, Effects of grain boundary engineering on the microstructure and corrosion fatigue properties of 316L austenitic stainless steel, *Front Mater [Internet]* 9 (2022), <https://doi.org/10.3389/fmats.2022.931848> [cited 2026 Mar 18].